CHINESE OPTICS LETTERS

Vol. 22, No. 3 | March 2024

Recent progress in thin-film lithium niobate photonic crystal [Invited]

Rui Ge (葛 睿)[1,†], Jiangwei Wu (吴江威)[1,†], Xiangmin Liu (刘翔敏)[1], Yuping Chen (陈玉萍)[1,2,*], and Xianfeng Chen (陈险峰)[1,3,4]

[1] State Key Laboratory of Advanced Optical Communication Systems and Networks, School of Physics and Astronomy, Shanghai Jiao Tong University, Shanghai 200240, China

[2] School of Physics, Ningxia University, Yinchuan 750021, China

[3] Shanghai Research Center for Quantum Sciences, Shanghai 201315, China

[4] Collaborative Innovation Center of Light Manipulations and Applications, Shandong Normal University, Jinan 250358, China

[†] These authors contributed equally to this work.

*Corresponding author: ypchen@sjtu.edu.cn

Received September 14, 2023 | Accepted November 30, 2023 | Posted Online February 20, 2024

Lithium niobate is a material that exhibits outstanding electro-optic, nonlinear optical, acousto-optic, piezoelectric, photorefractive, and pyroelectric properties. A thin-film lithium niobate photonic crystal can confine light in the sub-wavelength scale, which is beneficial to the integration of the lithium niobate on-chip device. The commercialization of the lithium niobate on insulator gives birth to the emergence of high-quality lithium niobate photonic crystals. In order to provide guidance to the research of lithium niobate photonic crystal devices, recent progress about fabrication, characterization, and applications of the thin-film lithium niobate photonic crystal is reviewed. The performance parameters of the different devices are compared.

Keywords: lithium niobate; photonic crystal; integrated optics.

DOI: 10.3788/COL202422.033602

1. Introduction

Lithium niobate ($LiNbO_3$, LN) is an outstanding ferroelectric material belonging to the $3m$ point group, and its refractive index (RI) is about 2.2[1]. It has a wide transparent window, high second-order nonlinearity, and stable physical and chemical characteristics[1,2]. A photonic crystal (PhC) can confine light at the sub-wavelength scale, and a PhC cavity has a high quality factor (Q-factor) and a small mode volume, which is beneficial for photonic nonlinear processes[1]. The development of the lithium niobate on insulator (LNOI) technique and the commercialization of the thin-film lithium niobate (TFLN) chip have promoted the realization of high-quality devices based on a lithium niobate photonic crystal (LNPhC). The integrated LN device[3–6], domain engineering based on LN[7], and the nonlinear LN device[8,9] have been reviewed thoroughly in previous research. However, a summary about LNPhCs, including their fabrications and applications, is absent yet. We believe that in the future the LNPhCs can be applied into the on-chip devices, as shown in Fig. 1, where the modulator, optomechanical cavity, sensor, and wavelength converter can be interconnected.

In this work, we review recent progress regarding the thin-film lithium niobate photonic crystal (TF-LNPhC). In Section 2, we attempt to emphasize the unique technique of etching holes with small sizes in LN. Then, several works about LNPhC band analysis and LNPhC cavities are reviewed. In Section 4, the LNPhC-based nonlinear devices, sensor, modulator, and optomechanics are discussed. For each device, the general working principle is illustrated. A few works about LN metasurfaces are briefly discussed. In Section 5, we attempt to emphasize the problems that result from imperfect etched holes.

2. Fabrication and Characterization of the LNPhC

The vital part of the research about the LNPhC is the fabrication process. When designing the LNPhC with the finite thickness, the light line is usually designed to be steep so that enough guided mode below the light line can be obtained. The steep light line can be realized by increasing the RI difference between the LN and the environment[10]. Before the LNOI boom, most studies focused on bulk LN. As early as 2003, Restoin *et al.* used

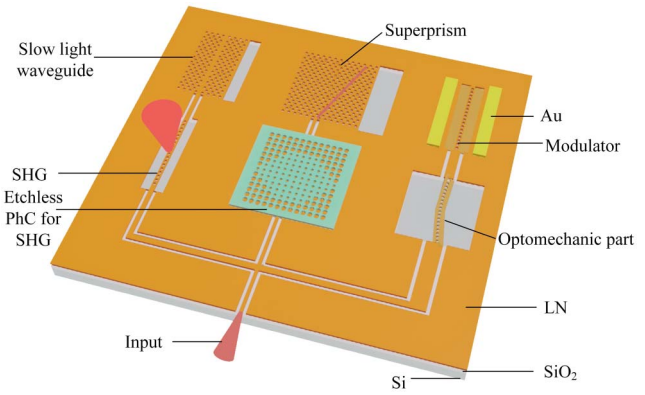

Fig. 1. Schematic of integrated LNPhC devices, including wavelength converter, sensor, modulator, opto-mechanical cavity, and superprism.

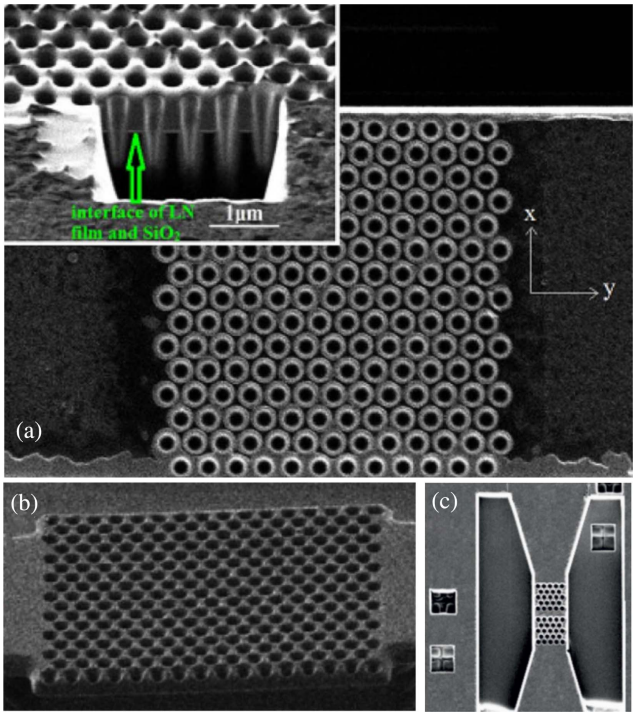

Fig. 2. Schematic of (a) TF-LNPhC on silica. Adapted with permission from [20]. (b) Suspended LNPhC. Adapted with permission from [22]. (c) APE LNPhC on common LN with lateral confinement. Adapted with permission from [15].

electron beam bombardment with wet etching for fabricating numerous shallow holes in bulk LN while the lattice constant was extremely large[11]. Then, researchers focused on the TF-LNPhC that is not surrounded by air[12–15], like annealed proton exchange (APE) LN slab on bulk LN. The development of the LNOI boosted the fabrication process of the high-quality LNPhC. With LNOI, researchers can dissolve the silica substrate using hydrofluoric (HF) acid, and the LNPhC is surrounded by air (self-suspended). Then, focused ion beam (FIB) and electron beam lithography (EBL), together with Ar^+ plasma etching, became popular for fabricating TF-LNPhC. Each method has advantages and disadvantages.

FIB is the most popular technique for fabricating the TF-LNPhC. In 2005 Lacour *et al.* fabricated the nanoscale holes on bulk LN and the lattice constant was at the sub-micrometer scale. Then, they characterized the fabricated LNPhC[16,17]. During the FIB process, the sample surface must be metallised and grounded to avoid charge accumulation[16]. The common masks are Cr[16] and Au[18] layers. The selected ion is Ga^+, and the accelerating voltage is 30 kV. FIB will result in a conical hole, which is due to material redeposition on the sidewalls when milling. Lu *et al.* proposed a method that can produce self-suspended TF-LNPhC. They created the air window by FIB and then etched the holes. Consequently, the LN layer became suspended[19]. As the LNOI became popular, researchers began to directly etch holes in the LNOI. The holes made by probe currents of 120 pA[20,21] and 90 pA[22] were obtained, and the corresponding characterizations were also performed[20–24]. In Fig. 2, we show some images of the LNPhC fabricated by FIB[15,20,22].

The drawback of FIB is that it is only suitable for the fabrication of small area structures (less than 50 × 50 holes). When fabricating large fields of photonic structures, long process times are required, and it can eventual drift[25].

Besides the two-dimensional (2D) LNPhC, FIB can also be used to fabricate a three-dimensional (3D) LNPhC. Courjal *et al.* first tilted the LN ridge with an angle of 90°. Then, they etched several grooves[26]. The holes are etched through the entire width of the ridge. The 3D LNPhC consists of several 2D TF-LNPhCs aligned along the *z*-direction.

The EBL, together with Ar^+ plasma etching, is an important technique for fabricating large number of TF-LNPhCs. It allows for patterning on the wafer scale[10]. The photo-resist can be selected as ZEP-520[27–30] or hydrogen silsesquioxane (HSQ)[31–34]. When using ZEP-520, an over-etching process can be used for producing a smooth sidewall. After over-etching, the slab thickness is decreased. When HSQ is used, the LN can be thinned to a smaller thickness by Ar^+ plasma at the first step[33]. Researchers have achieved 60°[34], 70°[35], and 85°[28] sidewall angles of the holes by using this method. In Fig. 3, we show some images of the LNPhC fabricated by EBL with Ar^+ etching[28–30].

To obtain the LNPhC with the high-quality holes, many researchers introduced extra nano-fabrication processes. Ulliac *et al.* proposed a method to etch holes in bulk LN that combines reactive ion etching and proton exchange, as shown in Fig. 4(a)[25]. The side wall angle can attain 85°[25]. Hartung *et al.* introduced the ion beam enhanced etching (IBEE) technique into the fabrication process of the holes of the LN[10]. The basic principle is also demonstrated in Fig. 4(a)[10]. The IBEE technique can etch holes with high aspect ratios and the low surface roughnesses on bulk LN on a large scale, while the side wall angle can attain 90°. The TF-LNPhC can be realized by using a buried damaged layer. The technique is based on the reduction of the chemical resistance of the crystal due to ion irradiation-induced defects. If the level of damage exceeds a specific

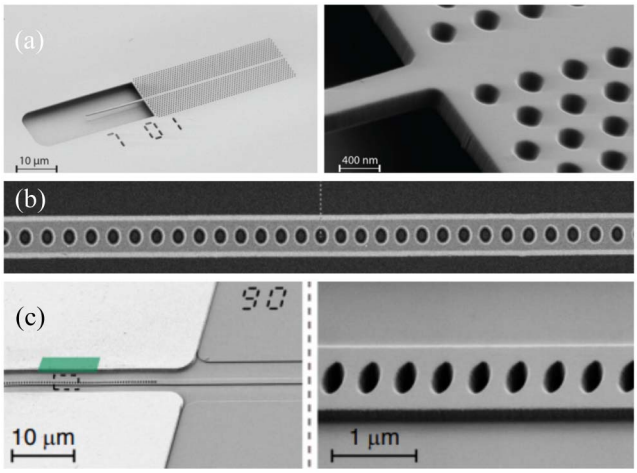

Fig. 3. Schematic of the LNPhC fabricated by EBL with Ar^+ etching. (a) 2D LNPhC cavity. Adapted with permission from [28]. (b) LNPhC cavity with ultra-high *Q*-factor. Adapted with permission from [29]. (c) LNPhC modulator. Adapted with permission from [30].

threshold, then the material can be removed by wet etching in diluted hydrofluoric acid. One drawback of this technique is that it requires that the optical axis of the LNPhC be parallel to the waveguide direction. To verify the feasibility of this technique, Geiss *et al.* characterized the LNPhC made by IBEE, and the experimental results agree with the simulation results[36]. Deng *et al.* verified that during the IBEE process, the LNPhC can be fabricated by FIB without EBL, and the ion implantation becomes the first step. Moreover, HF wet etching is used to produce the air gap and the steep side wall. The selected beam current is 100 pA, and the formed air gap is 250 nm. Finally, they characterized the fabricated TF-LNPhC, and the Fano resonance is observed[18,37]. The LNPhC cavity made by using the IBEE technique shows the high *Q*-factor mode and thus can be used for second-harmonic generation[38,39]. The potassium hydroxide assisted IBEE method is also used to fabricate the TF-LNPhC[40].

Calero *et al.* proposed the redeposition-free FIB etching technique[41]. They noted that the fabrication imperfections during the FIB process are owing to the large hole conicity, thickness erosion, and surface roughness. Moreover, the FIB image may also damage the fabricated structure. To improve the surface quality, they used a small probe current (24 pA). To obtain holes with a quasi-cylindrical shape, they added extra processes[41]. They simulated the Fano resonance based on the LNPhC, and the experimental results show good coincidence with the simulated one. Qu *et al.* improved this method, as shown in Fig. 4(b), and fabricated the TF-LNPhC where the second-harmonic signal can be observed[42]. Compared with directly etching holes in the TFLN using FIB, the redeposition-free FIB etching technique added the prefabrication process, including etching the Si layer at the back of the TFLN layer, which created the air region. Owing to the existence of the air region, the Ga^+ ion can enter the free space directly, which avoids material redeposition[42]. In Fig. 4(c), we show the SEM images of the holes in the TFLN made by using the IBEE and redeposition-free FIB techniques[36,42].

Owing to the fact that the fabrication process of the LNPhC with the high-quality holes is usually costly, researchers recently began to focus on the LN layer with the etched mask, while the TFLN itself is not etched. The architecture is defined as "etchless LNPhC" and does not require the complicated fabrication process, as shown in Fig. 5[43,44]. The hybrid integration of the TFLN with a PhC based on other materials, combines the excellent property of the LN and the band-gap property of other materials[43]. Moreover, some etchless LNPhCs are based on bound states in the continuum (BIC)[44].

Another method of fabricating LNPhC is laser writing-assisted LN nanolithography. In 2008, Ishikawa *et al.* obtained the LNPhC by direct laser fabrication with 150 fs pulses at 767 nm, and the diameters of the fabricated cone-shaped holes in the bulk LN are at the micron scale[45]. In general, the diameter of holes in LN fabricated by direct laser writing is relatively larger than the one fabricated by FIB or Ar^+ plasma etching[45]. However, Wang *et al.* found that once combining femtosecond-laser writing with other techniques like wet etching, holes with a small size (100 nm) and a high aspect ratio can be obtained[46,47].

Currently, there are four popular characterization methods of the LNPhC: tapered fiber coupling[27], end-face coupling[15], cross-polarized resonant scattering coupling[38], and grating coupling[34]. The schematics of these characterization methods are shown in Fig. 6[15,28,34,38]. The basic principles of these coupling methods are similar with those in the silicon PhC. The coupling efficiency inside the cavity of the cross-polarized resonant scattering method is estimated to be 20%[38]. While for the grating coupling, owing to the difficulties of simultaneously etching the grating couplers and holes, more than one EBL, together with dry-etching processes, are required[34].

3. Band Analysis, Cavity, and Slow Light Waveguide Based on LNPhCs

When designing the LNPhC, the prerequisite is to obtain a wide band gap. Rolland *et al.* simulated the photonic and phononic band properties of the LNPhC with various lattice arrangements and thicknesses[48]. They found that a simultaneous photonic and phononic band gap exists as the parameters are finely tuned. The triangle lattice with a suitable thickness and radius will lead to the wide photonic band gap[48]. Li *et al.* also obtained the band property of the erbium-doped LNPhC, and the band gap can exist[49]. Sivarajah *et al.* pointed out that, owing to the anisotropism of LN, the analysis approach of the LNPhC band diagram is different from the traditional PhC[50].

Owing to the low RI of LN, designing a high-*Q* cavity based on the LNPhC is challenging[51]. However, many state-of-the-art works successfully obtained ultra-high *Q*-factors both in simulation and experiment, as shown in Table 1. Most of them are based on a mode-gap cavity (heterostructure cavity)[55], where the lattice constants are gradually changed along the line defect. The physical mechanisms of the high-*Q* factor in the

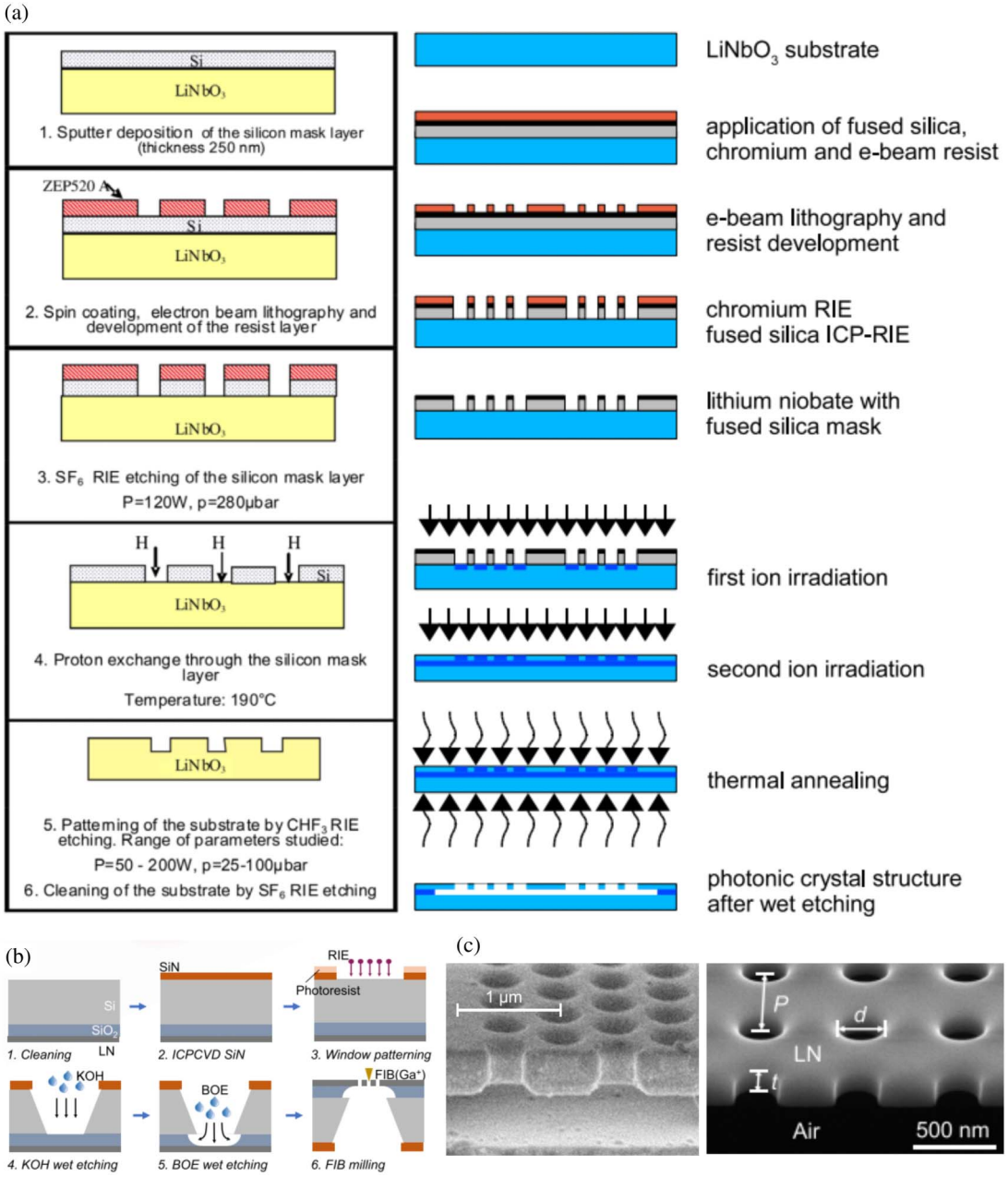

Fig. 4. (a) Fabrication procedures of LNPhC based on the reactive ion etching and the IBEE technique. Adapted with permission from [10] and [25]. (b) Fabrication procedure of LNPhC based on redeposition-free FIB technique. Adapted with permission from [42]. (c) SEM image of holes fabricated by IBEE technique and redeposition-free FIB technique. Adapted with permission from [10] and [42].

heterostructure cavity are discussed in previous work that used a silicon PhC[56,57]. Except for the Q-factor, the modal volume of the cavity is also gradually decreased. The modal volume of $0.78\ (\lambda/n)^3$ is obtained with an ultra-high Q-factor[29]. An interesting trait of the LNPhC cavity is the saturation and quenching of the photorefraction effect[27]. The resonant wavelength of the cavity changes when the input power increases owing to the photorefractive effect. As the input power attains a certain value, the resonant wavelength of the cavity no longer varies. That is to say, the cavity attains a saturation state. However, when the input power maintains this value for some time, the resonant wavelength will move back to its initial value[27].

A slow light waveguide has strong light–matter interaction and thus can enhance the nonlinear process. The research of the LNPhC slow light waveguide began from the bulk LNPhC. Iliew *et al.* used a bulk LNPhC to illustrate that the bulk bands can be used for phase matching. Utilizing the conjugated form of the Lorentz reciprocity theorem with related FDTD simulation, they verified that once the phase-matching condition is satisfied, the effective area is negatively correlated with the group

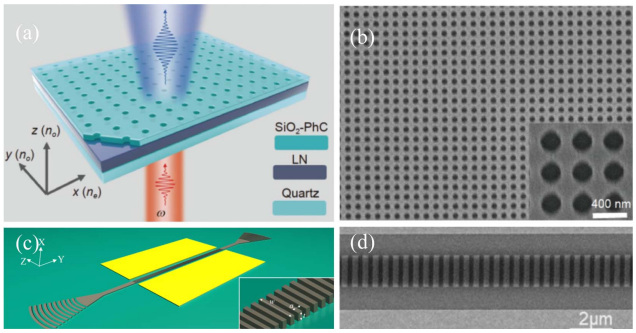

Fig. 5. (a) Schematic and (b) SEM image of the etchless LNPhC with silica as the mask. Adapted with permission from [43]. (c) Schematic and (d) SEM image of the etchless LNPhC with polymer as the mask. Adapted with permission from [44].

index, while the nonlinearity can be determined by the effective area[58,59].

4. Application of the LNPhC

4.1. Nonlinear frequency conversion

4.1.1. Parametric up-conversion

Owing to the predominant nonlinear property of LN and the small modal volume of the PhC slab, the TF-LNPhC cavity or slow light waveguide give birth to the high-efficiency parametric up-conversion process[1]. The SHG (second-harmonic generation) efficiency is experimentally proved to be sensitive to the incident polarization angle and the direction of optical axis[38]. The SHG efficiency is quadratically dependent on the intracavity power, i.e., $(QT^{0.5}/V)^2$[52]. This implies that the LNPhC cavity with a high Q/V can generate more second-harmonic waves. For the L3 cavity, the SHG efficiency is 6.4×10^{-9}[38]. Owing to the fact that the cavity with a Q-factor of 10^6 is successfully obtained experimentally, the appreciable second-harmonic waves and even third-harmonic waves are observed. The SHG efficiency is 0.078% W^{-1}[28]. The sum-frequency generation is also observed[53]. The second-harmonic waves can also be excited by the pulse source and the SHG efficiency is 2×10^{-4}[42].

The generated second-harmonic signal can be collected directly by the tapered fiber, while the fiber is usually designed for the telecom band and may show low efficiency at the second-harmonic band[28]. The second-harmonic signal can also be reflected by the dichroic mirror spatially and collected by the silicon avalanche photodiode[38]. For a singly resonant LNPhC cavity, the generated second-harmonic waves are usually free-space radiated[52], which is different from that in the LN microdisk cavity[60,61]. Introducing BIC into the second harmonic wavelength will lessen the radiating angle[62]. More recently, the LN metasurface has become another popular platform for observing second-harmonic waves[63,64]. In Fig. 7, some results about parametric up conversion based on LNPhC are exhibited[28,38,42].

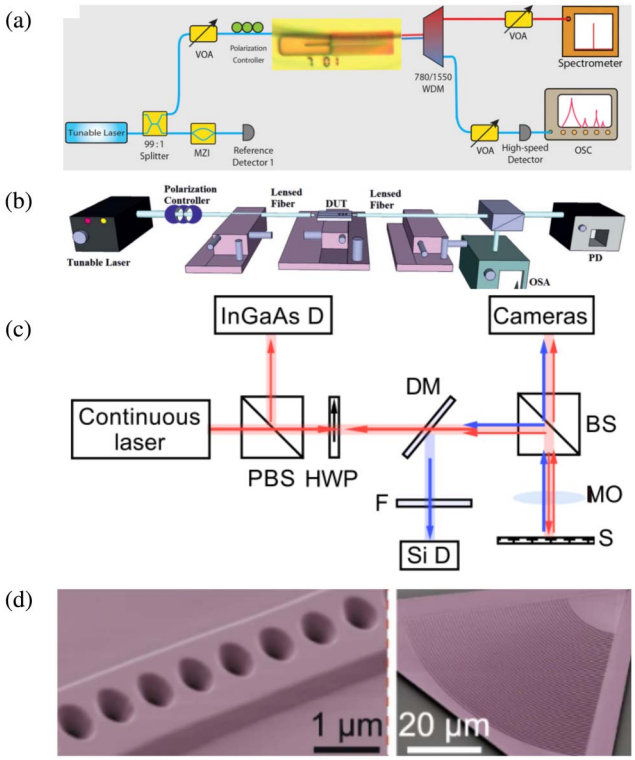

Fig. 6. (a) Schematic of tapered fiber coupling. Adapted with permission from [28]. (b) End-face coupling. Adapted with permission from [15]. (c) Cross-polarized resonant scattering coupling. Adapted with permission from [38]. (d) Grating coupling. Adapted with permission from [34].

The SHG based on the thin film LN slow light waveguide is also an important direction. For the bulk LNPhC, the effect of the light line is often ignored owing to the infinite thickness. That is to say, the modes at both the fundamental wavelength and the second-harmonic wavelength are lossless[65]. As a result, the power of the generated second-harmonic waves increases with the propagation distance once the phase-matching condition is satisfied[60]. However, the relevant theory cannot extend to the waveguide in the PhC slab since the mode at the second-harmonic wavelength usually locates beyond the light line[65]. Saravi *et al.* proposed a method that can match a slow light mode with a leaky mode[65]. They considered the condition that the fundamental mode is lossless, but the second-harmonic mode is lossy owing to the existence of the light line. They used adjoint field formalism to illustrate the mechanism and verified their hypothesis by using a slow light waveguide on a TF-LNPhC using the FDTD method. As the pump waves propagate along the path, the second-harmonic waves attain the saturation value, which means that the generated SH power gradually balances with the radiating SH power. The efficiency is 8×10^{-5} W^{-1}. Then, they investigated the influence of the loss of the fundamental mode on the behavior of the second-harmonic waves in a TF-LNPhC nanobeam[66]. Using the same theory and assuming that the phase-matching condition is satisfied, they found that when both the fundamental mode and second-harmonic

Table 1. *Q*-Factors of the Recent Works Based on the TF-LNPhC Cavity.

Ref.	Cavity Type	*Q*-factor	Fabrication Method	Year
[38]	L3	775 (Sim.), 535 (Exp.)	IBEE	2013
[52]	Mode-gap	3.9×10^6 (Sim.)	–	2015
[21]	Mode-gap	330 (Sim.), 156 (Exp.)	FIB	2016
[27]	Mode-gap	6×10^6 (Sim.), 1.09×10^5 (Exp.)	EBL + Ar^+ etching	2017
[53]	Mode-gap	5.43×10^4 (Exp.)	EBL + Ar^+ etching	2018
[28]	Mode-gap	1.5×10^6 (Sim.), 3.51×10^5 (Exp.)	EBL + Ar^+ etching	2019
[29]	Mode-gap	1.23×10^8 (Sim.), 1.41×10^6 (Exp.)	EBL + Ar^+ etching	2019
[31]	Mode-gap	4×10^6 (Sim.), 3.5×10^5 (Exp.)	EBL + Ar^+ etching	2019
[51]	L4/3 with inverse design	9.7×10^6 (Sim.)	–	2020
[54]	Mode-gap	6.29×10^4 (Exp.)	EBL + Ar^+ etching	2020
[30]	Mode-gap	1.34×10^5 (Exp.)	EBL + Ar^+ etching	2020
[32]	Mode-gap	1.7×10^4 (Exp.)	EBL + Ar^+ etching	2020
[33]	Mode-gap	4.7×10^5 (Exp.)	EBL + Ar^+ etching	2020
[42]	Bulk	75 (Exp.)	Redeposition-free FIB	2022
[44]	BIC	12,010 (Exp.)	Etchless LNPhC	2022
[34]	Mode-gap	1.58×10^5 (Exp.)	EBL + Ar^+ etching	2023

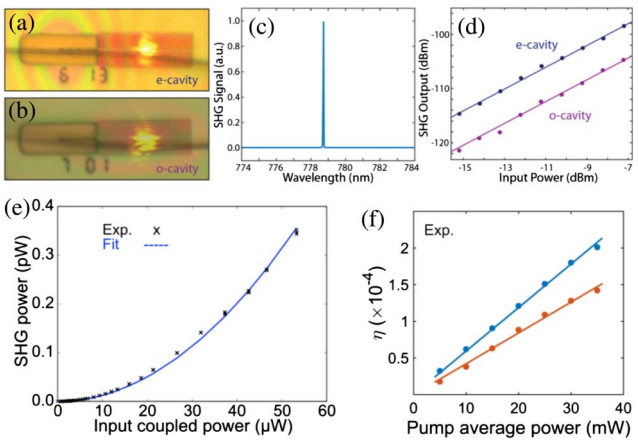

Fig. 7. (a), (b) Optical microscopy images of two different mode-gap cavities. (c) Spectrum of the second-harmonic signal of the mode-gap cavity. (d) Second-harmonic power as a function of the fundamental pump wave power of the mode-gap cavity. Adapted with permission from [28]. (e) Second-harmonic power as a function of the fundamental pump wave power of the L3 cavity. Adapted with permission from [38]. (f) Second-harmonic power as a function of the fundamental pump wave of the bulk cavity made by redeposition-free FIB. Adapted with permission from [42].

mode are lossy, it will reach a peak value and then drop as the propagation distance increases monotonously due to the fact that the generated second-harmonic wave cannot balance the pump wave[66].

4.1.2. Parametric down-conversion

In addition to the parametric up-conversion process, the TF-LNPhC also shows potential in the parametric down conversion area. Saravi *et al.* designed a double-slot PhC slow light waveguide based on TFLN. The field of the Bloch mode of the PhC can be expanded into Bloch harmonics, and the introduction of the slow light waveguide can increase the efficiency of the nonlinear process that involves the non-dominant Bloch harmonic mode[67]. Additionally, by phase-matching a forward-propagating pump mode and a high-order signal/idler mode with a backward-propagating low-order idler/signal mode, the path-entangled photon pairs by spontaneous parametric down-conversion are realized[67]. After that, they use a similar structure and methodology to generate spectrally unentangled biphoton states, which shows potential in the heralding of single photons[68]. The schematic is shown in Fig. 8[68]. The key point of producing factorizable pairs is to satisfy the group index relationship of the pump, idler, and signal modes. Finally, the calculated joint phase-matching spectrum verified the hypothesis.

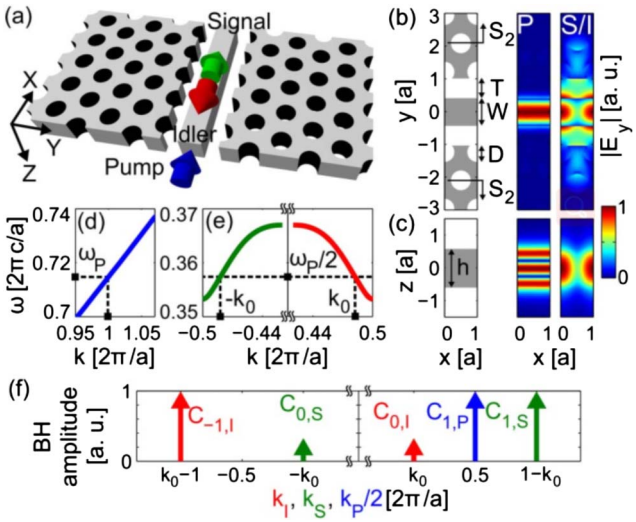

Fig. 8. (a) Schematic of the LNPhC waveguide used for generating spectrally unentangled biphoton states. Mode profiles of pump, signal, and idler modes at the (b) $z = 0$ and (c) $y = 0$ planes. (d) Band diagram of the pump mode. (e) Band diagram of the signal and idler modes. (f) Bloch harmonic distribution of the modes. Adapted with permission from [68].

However, these works are all based on perturbative analyses or simulations while the corresponding experiments are lacking. Once a relative device is fabricated and the characterization is boosted, a more colorful parametric down-conversion process can be realized on the LNPhC platform.

4.2. Sensor

Owing to the large Pockels coefficient and outstanding pyroelectric property[1], LN is the exceptional platform for constructing a sensor. Sensors with high quality based on the LN nanotube[69], LN microdisk[70], and LN waveguide[71] have already been demonstrated. The sensor based on the LNPhC began from the superprism in the bulk material[72]. As for the sensor based on the TF-LNPhC, it mainly depends on the response of the high-Q resonance peak against environments. The deviation of the LN RI can be estimated by[19]

$$\Delta n = -\frac{1}{2} n_e^3 f^2 r_{33} E_z, \tag{1}$$

where n_e is the extraordinary RI of LN, and E_z is the electric field brought by an electrode or pyroelectric effect. r_{33} is the electro-optic coefficient, and f is the optical field factor. It can be calculated by[73]

$$f = \frac{\iiint_{\mathrm{PhC}} |E(x,y,z)| \mathrm{d}x\mathrm{d}y\mathrm{d}z}{\iiint_{\mathrm{bulk}} |E(x,y,z)| \mathrm{d}x\mathrm{d}y\mathrm{d}z}. \tag{2}$$

The above formulas are also utilized in the LNPhC modulator. To obtain the high-quality LNPhC sensor, some special mechanisms are introduced. The slow light waveguide can be used to construct the sensor because of its enhanced light–matter interaction. Lu *et al.* designed a slow light waveguide on the TF-LNPhC in experiment[19]. The structure supports the slow light mode, which can form a resonant peak. The peak moves as the temperature varies by the Peltier element. The sensitivity of the sensor is 0.359 nm/°C. The Fano resonance is sensitive to the environmental change[74]. The temperature sensor based on the Fano resonance is realized. It is constructed by the TF-LNPhC without etching the silica layer[75]. The Fano resonance is generated by the superposition of the guided modes on the LN slab with the background signal. The sensitivity is 0.77 nm/°C. When the temperature is high, the resonance wavelength shift becomes nonlinear owing to the elastic deformation. The Fano resonance-based LNPhC electric field sensor exhibits the sensitivity of 50 μV/m in simulation[76]. After that, Qiu *et al.* theoretically constructed a one-dimensional TF-LNPhC as the electric field sensor, and the minimum detectable electric field is 23 mV/m[73]. The lab-on-fiber technology can inscribe the device within the ultra-small volume, and it is used to build a LNPhC sensor on a fiber experimentally[77,78]. Ma *et al.* simulated an etchless LNPhC sensor, and the sensitivity is 3 pm/°C. They etched the TiO_2 and claimed that it can compensate the thermal effects induced by the LN[79]. Bound state in the continuum (BIC) exhibits the large Q-factor which can benefit the sensor. The LNPhC sensor based on the BIC can detect the minimum electric field of 25 μV/m[80]. Panda *et al.* simulated a sucrose sensor constructed by using a one-dimensional LNPhC. The upper and lower edge wavelengths of the band gap gradually change when the LNPhC is immersed in different sucrose concentrations. The limit of detection is 2.28×10^{-4} RIU, and the sensitivity is 1016.35 nm/RIU[81]. In Fig. 9, some transmission spectra of the LNPhC sensor are exhibited[75,80].

4.3. Electro-optic modulator

Electro-optic modulators translate electrical signals to light, and LN has been the outstanding material to construct modulators[82,83]. LNPhC modulators are usually small in size compared with the LN waveguide modulator[84]. Researchers investigated the electro-optic properties of the APE TF-LNPhC and the common TF-LNPhC[15]. The response of the APE TF-LNPhC under the radio frequency is obtained. Lu *et al.* proposed an LNPhC modulator based on the APE TF-LNPhC, and the performance parameters of the device are obtained experimentally. The electrodes are sputtered on the side of the LNPhC, and the radio frequency generator is connected with it[84]. Li *et al.* proposed an LNPhC modulator based on the LNPhC nanobeam, and they pointed out that the modulator can be used for high-speed electro-optic switching, as shown in Fig. 10[30]. At a modulation frequency that is much smaller than the cavity linewidth, increasing the driving power simply broadens the transmission spectrum. When the modulation frequency is greater than the cavity linewidth, the frequency conversion of photons into sidebands with frequency separation is equal to the modulation frequency. Then, they applied the signal with a pseudo-random binary sequence to the modulator. The open eyes can be seen. The bit-switching energy is 22 fJ.

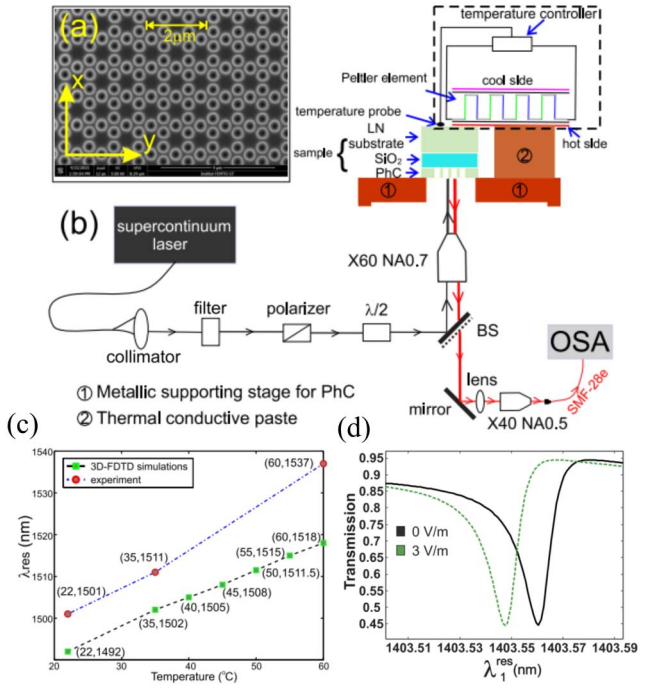

Fig. 9. (a) SEM image, (b) experimental setup, and (c) results for Fano resonance-based LNPhC sensor. Adapted with permission from [75]. (d) Simulated transmission of the BIC LNPhC sensor. Adapted with permission from [80].

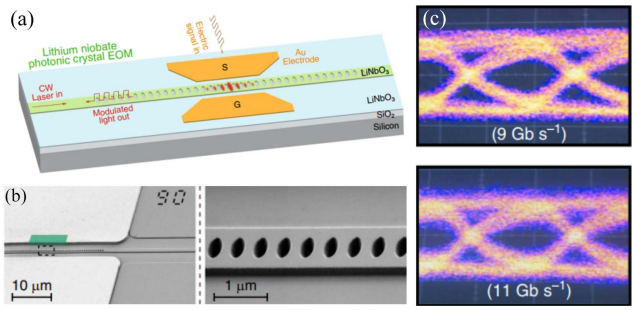

Fig. 10. (a) Structure and (b) SEM image and enlarged SEM image of the mode-gap LNPhC modulator. (c) Eye diagrams of the electro-optic switch. Adapted with permission from [30].

Following these works, modulators based on the etchless LNPhC waveguide[44], LN nanobeam on silica[85], and the fishbone gratings are designed[86]. Deng *et al.* mentioned that the modulation efficiency can be estimated by a theoretical formula that involves the effective index of the optical mode[86]. In Table 2, we show the performance parameters of these works.

4.4. Optomechanics

LN has a high piezoelectric coefficient. Suspended LN thin films can achieve a high acoustic frequency and a large *Q*-factor. The one-dimensional LNPhC nanobeam is an excellent platform for investigating the optomechanic phenomenon, and it can also be defined as "optomechanical crystal"[31]. The laser wavelength can be locked halfway into the cavity resonance, and the power spectrum of the cavity can be monitored by a real-time spectrum analyzer[57]. Researchers have successfully monitored the power spectra, which exhibit mechanical modes with high *Q*-factors. The mechanical lasing and the high-order harmonic oscillation are observed experimentally. The requirements of the mechanical lasing can be derived from the interaction Hamiltonian. As the optomechanical cooperativity reaches the threshold value, the LNPhC begins to oscillate, and a mechanical lasing peak emerges[31]. The coupling type can be distinguished by the mechanical resonance shape. The investigations about optomechanics on the LNPhC nanobeam platform can benefit high-quality transducers or actuators[32,33]. The merit lies in the fact that the microwave-to-mechanical conversion efficiency is significantly increased. In Fig. 11 and Table 3, we show some state-of-the-art designs of the LN optomechanical crystal[27,31,33,54].

After reviewing the applications of the LNPhC, we can summarize two main advantages of LNPhC devices compared with LN devices based on other structures. One advantage is the smaller modal volume and smaller footprint. Owing to the ability of confining photons at the sub-wavelength scale, the size of the LNPhC device is small, which is beneficial for integration. For example, the footprint of the TF-LNPhC temperature sensor is 25 μm × 24 μm[75], which is much smaller than the LN microdisk temperature sensor with a diameter of 50 μm[70]. Another advantage of the LNPhC is the ability of band engineering. This

Table 2. Performance Parameters of the Modulator Based on the TF-LNPhC[a].

Ref.	Modulator Structure	$V_\pi \cdot L$ (V · cm)	V_π (V)	L (mm)	3 dB Bandwidth (GHz)	Sim./Exp.	Year
[87]	MZI	–	0.66	–	100	Sim.	2013
[84]	Slow light waveguide	0.0063	11.8	0.0053	1	Exp.	2014
[30]	Nanobeam	–	–	–	17.5	Exp.	2020
[44]	Etchless waveguide	–	–	–	28	Exp.	2022
[85]	Nanobeam	0.0874	10	0.0874	600	Sim.	2022
[86]	Nanobeam	1.42	–	–	80	Sim.	2023

[a]Sim., simulation; Exp., experiment.

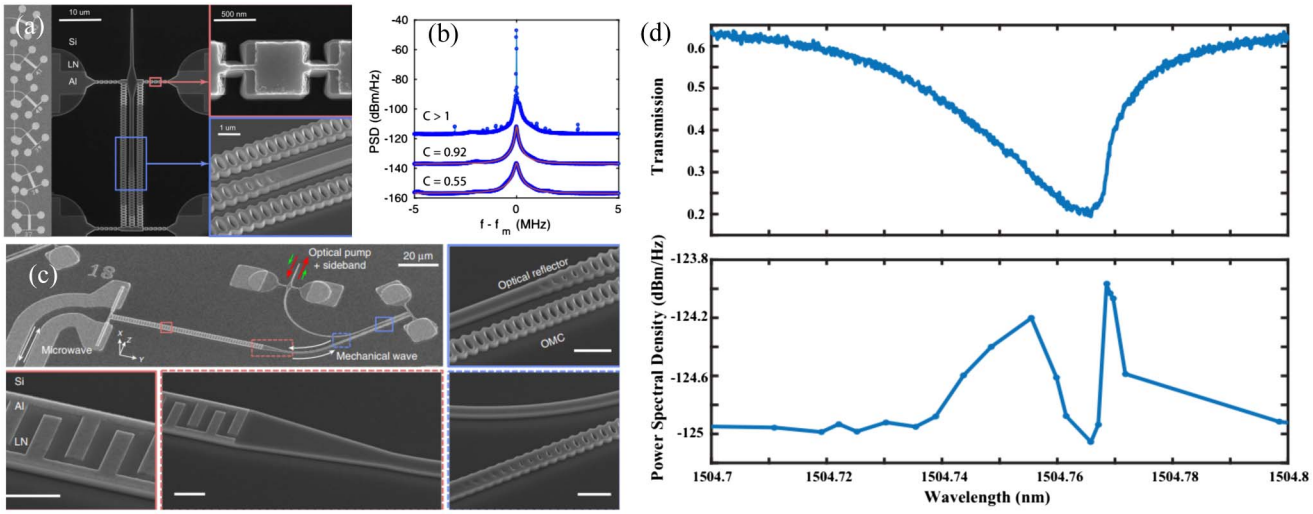

Fig. 11. (a) SEM image of suspended LNPhC nanobeam and (b) observed mechanical lasing. Adapted with permission from [31]. (c) SEM image of the LNPhC transducer. Adapted with permission from [33]. (d) Transmission spectrum and power spectral density change for the mechanical mode. Adapted with permission from [54].

Table 3. Optomechanic Properties of the LNPhC Nanobeam for Some State-of-the-Art Experimental Works.

Ref.	*Q*-factor (Optical)	*Q*-factor (Mechanical)	Coupling Rate	Year
[27]	1×10^5	6192	71 kHz	2017
[31]	3×10^5	17,000	120 kHz	2019
[54]	6.3×10^4	65	–	2020
[32]	1.7×10^4	20	–	2020

merit leads to colorful physical phenomena like slow light[65] and the superprism effect[72].

5. Challenges

Although the fabrication processes of the LNPhC have improved conspicuously over the years, the technique that etches the high-quality holes at the expense of the low cost is still absent. Owing to the stable physical and chemical characteristics, traditional techniques produce conical holes with sidewall angles of 55°–85°. The conical holes will degrade the photon confinement in the LNPhC, whether it is composed of a bulk structure or a slab. The RI of the LN is small compared with silicon, and as a result, the LNPhCs usually are self-suspended, which increases requests for the etching process. Burr *et al.* have theoretically and experimentally pointed out that in bulk LNPhCs it is difficult for conical holes of any depth to produce well-defined stop bands. The band diagram of the conical holes suggests a superposition of many different band diagrams corresponding to the different r/a ratios, and the band gap is hard to distinguish. Moreover, the field distribution indicates that the incident light is refracted towards the bottom of the substrate, which verifies the absence of the well-defined band gap[88]. Yavuzcetin *et al.* have investigated the transmission property of Bragg gratings. The gratings are constructed with the APE LN ($n = 2.148$) slab while it stands on the bulk LN ($n = 2.138$). The phenomenon that the incident light is refracted towards the bottom of the substrate can also be observed[89–91]. For the PhC slab, the non-steep side wall of the holes will mix the TE and the TM modes, which also weaken the photon confinement[92].

The IBEE technique and the redeposition-free FIB technique can etch the high-quality holes with a sidewall angle of 90° but are costly. Some etchless PhCs are based on structured photoresist, utilizing the BIC, which requires that the arrayed holes be identical, adequate, and with the fixed lattice arrangement to obtain a high *Q*-factor. Meanwhile, no defects can be introduced. These requirements limited the flexibility of the design. Other etchless PhCs require heterogeneous integration while the holes are etched in the non-LN materials. The process may require extra procedures.

In Table 4, we show the performance comparison of different fabrication processes of the TF-LNPhC.

6. Conclusion and Perspective

In conclusion, the fabrication, the characterization, and the applications of the TF-LNPhC are reviewed. As we formerly mentioned, the challenge of the TF-LNPhC lies in the difficulty of fabricating a nanostructure, like the non-steep sidewall. Meanwhile, the area and length of the suspended structure-like cavity are limited, which results in a low *Q*-factor. State-of-the-art fabrication techniques may solve this problem. Many fabrication approaches that are already used to construct LN

Table 4. Comparison of Different Fabrication Processes of TF-LNPhC.

Method	Sidewall Angle (°)	Etching Technique of Holes	Fabrication Scale
FIB	Near 83	Ga^+ milling	Small scale
EBL + Ar^+ plasma etching	55–85	Ar^+ milling	Wafer scale
Redeposition-free FIB	Near 90	Ga^+ milling	Small scale
IBEE	90	HF wet etching	Wafer scale

micro-nanostructures (excluding the LNPhC) show potential for etching a hole array in the LN slab with high quality. One example is diamond-like carbon-assisted etching technique[93]. With the help of the plasma-enhanced chemical vapor deposition process, the diamond-like carbon mask is placed beyond the LN layer. By dry etching the structure is patterned on the mask. After the Ar^+ eching process, the pattern-like microring is transferred to the LN layer. The etched holes have a very steep sidewall[93]. This promising method etches microstructures at the large scale and can avoid ion irradiation. This shows potential for fabricating high quality TF-LNPhC devices. Another example is the femtosecond-laser writing-assisted wet etching technique[47], which has already been discussed in the former part. This method can also circumvent ion irradiation and has not been applied into the TF-LNPhC. Once the fabrication technique obtains breakthrough, the finely fabricated TF-LNPhC will show excellent regulating ability for dispersion relationship or photon confinement. This provides a versatile tool for controlling light and deepening our understanding of light–matter interactions. Over the years, numerous devices based on the TF-LNPhC have been proposed, and they enriched the diversity of the integrated LN photonic circuits. The research of rare earth ions doped LNPhC is still unpopular, although efforts are being made[34,94]. The LNPhC laser has not yet been designed, while LN microdisk lasers[95,96] and microring lasers[97] have been constructed recently. The development of rare earth ions doped LNPhC can also benefit the emergence of the non-Hermitian LNPhC. Owing to the excellent nonlinear property of LN, the LNPhC may show potential in topological photonic devices, which exhibit the nonlinear effect. Yan *et al.* designed the LN waveguide arrays and demonstrated that the rotating Wely point in the synthetic dimension can be realized[98]. The second-harmonic generation on the LNOI is used to probe the topological interface state. The photonic devices based on bulk LNPhCs[99,100] may also be designed by the TF-LNPhC in the future. Inverse design is another recent hot spot. Combining inverse design and the LNPhC cavity has successfully enhanced the *Q*-factor[51]. Introducing the inverse design into other LNPhC-based integrated devices may further upgrade their performance. In practical fabrication processes, different holes can show different sidewall angles, i.e., the sidewall angle of the holes is not a fixed value but shows fluctuations. One potential solution is introducing merged BICs, which is immune to fabrication imperfection[101]. Lastly, we hope this review can provide guidance to the design of high quality LNPhC devices.

Acknowledgements

This work was supported by the National Natural Science Foundation of China (Nos. 91950107, and 12134009), the National Key R&D Program of China (No. 2019YFB2203501), the Shanghai Municipal Science and Technology Major Project (No. 2019SHZDZX01-ZX06), and the SJTU (No. 21X010200828).

References

1. D. Zhu, L. Shao, M. Yu, *et al.*, "Integrated photonics on thin-film lithium niobate," Adv. Opt. Photonics **13**, 242 (2021).
2. Y. Qi and Y. Li, "Integrated lithium niobate photonics," Nanophotonics **9**, 1287 (2020).
3. A. Boes, B. Corcoran, L. Chang, *et al.*, "Status and potential of lithium niobate on insulator (LNOI) for photonic integrated circuits," Laser Photonics Rev. **12**, 1700256 (2018).
4. J. Lin, F. Bo, Y. Cheng, *et al.*, "Advances in on-chip photonic devices based on lithium niobate on insulator," Photonics Res. **8**, 1910 (2020).
5. Y. Kong, F. Bo, W. Wang, *et al.*, "Recent progress in lithium niobate: optical damage, defect simulation, and on-chip devices," Adv. Mater. **32**, 1806452 (2020).
6. Y. Jia, L. Wang, and F. Chen, "Ion-cut lithium niobate on insulator technology: recent advances and perspectives," Appl. Phys. Rev. **8**, 011307 (2021).
7. D. Sun, Y. Zhang, D. Wang, *et al.*, "Microstructure and domain engineering of lithium niobate crystal films for integrated photonic applications," Light Sci. Appl. **9**, 197 (2020).
8. S. Saravi, T. Pertsch, and F. Setzpfandt, "Lithium niobate on insulator: an emerging platform for integrated quantum photonics," Adv. Opt. Mater. **9**, 2100789 (2021).
9. Y. Zheng and X. Chen, "Nonlinear wave mixing in lithium niobate thin film," Adv. Phys. X **6**, 1889402 (2021).
10. H. Hartung, E.-B. Kley, T. Gischkat, *et al.*, "Ultra thin high index contrast photonic crystal slabs in lithium niobate," Opt. Mater. **33**, 19 (2010).
11. C. Restoin, S. Massy, C. Darraud-Taupiac, *et al.*, "Fabrication of 1D and 2D structures at submicrometer scale on lithium niobate by electron beam bombardment," Opt. Mater. **22**, 193 (2003).
12. M. R. Beghoul, B. Fougere, A. Boudrioua, *et al.*, "Photonic band gap grating in He^+-implanted lithium niobate waveguides," Opt. Quantum Electron. **39**, 333 (2007).
13. S. Diziain, S. Harada, R. Salut, *et al.*, "Strong improvement in the photonic stop-band edge sharpness of a lithium niobate photonic crystal slab," Appl. Phys. Lett. **95**, 101103 (2009).
14. F. Sulser, G. Poberaj, M. Koechlin, *et al.*, "Photonic crystal structures in ion-sliced lithium niobate thin films," Opt. Express **17**, 20291 (2009).

15. H. Lu, B. F. Issam, G. Ulliac, *et al.*, "Lithium niobate photonic crystal wire cavity: Realization of a compact electro-optically tunable filter," Appl. Phys. Lett. **101**, 151117 (2012).
16. F. Lacour, N. Courjal, M.-P. Bernal, *et al.*, "Nanostructuring lithium niobate substrates by focused ion beam milling," Opt. Mater. **27**, 1421 (2005).
17. M. Roussey, M.-P. Bernal, N. Courjal, *et al.*, "Experimental and theoretical characterization of a lithium niobate photonic crystal," Appl. Phys. Lett. **87**, 241101 (2005).
18. J. Deng, S. Hussain, V. S. Kumar, *et al.*, "Modeling and experimental investigations of Fano resonances in free-standing photonic crystal slabs," Opt. Express **21**, 3243 (2013).
19. H. Lu, B. Sadani, G. Ulliac, *et al.*, "Integrated temperature sensor based on an enhanced pyroelectric photonic crystal," Opt. Express **21**, 16311 (2013).
20. L. Cai, H. Han, S. Zhang, *et al.*, "Photonic crystal slab fabricated on the platform of lithium niobate-on-insulator," Opt. Lett. **39**, 2094 (2014).
21. L. Cai, S. Zhang, and H. Hu, "A compact photonic crystal micro-cavity on a single-mode lithium niobate photonic wire," J. Opt. **18**, 035801 (2016).
22. S.-M. Zhang, L.-T. Cai, Y.-P. Jiang, *et al.*, "High extinction ratio bandgap of photonic crystals in LNOI wafer," Opt. Mater. **64**, 203 (2017).
23. S. Diziain, R. Geiss, M. Steinert, *et al.*, "Self-suspended micro-resonators patterned in Z-cut lithium niobate membranes," Opt. Mater. Express **5**, 2081 (2015).
24. H. Lu, B. Sadani, G. Ulliac, *et al.*, "6-micron interaction length electro-optic modulation based on lithium niobate photonic crystal cavity," Opt. Express **20**, 20884 (2012).
25. G. Ulliac, N. Courjal, H. M. H. Chong, *et al.*, "Batch process for the fabrication of $LiNbO_3$ photonic crystals using proton exchange followed by CHF_3 reactive ion etching," Opt. Mater. **31**, 196 (2008).
26. N. Courjal, J. Dahdah, G. Ulliac, *et al.*, "Optimization of $LiNbO_3$ photonic crystals: toward 3D $LiNbO_3$ micro-components," Opt. Express **19**, 23008 (2011).
27. H. Liang, R. Luo, Y. He, *et al.*, "High-quality lithium niobate photonic crystal nanocavities," Optica **4**, 1251 (2017).
28. M. Li, H. Liang, R. Luo, *et al.*, "High-*Q* 2D lithium niobate photonic crystal slab nanoresonators," Laser Photonics Rev. **13**, 1800228 (2019).
29. M. Li, H. Liang, R. Luo, *et al.*, "Photon-level tuning of photonic nanocavities," Optica **6**, 860 (2019).
30. M. Li, J. Ling, Y. He, *et al.*, "Lithium niobate photonic-crystal electro-optic modulator," Nat. Commun. **11**, 4123 (2020).
31. W. Jiang, R. N. Patel, F. M. Mayor, *et al.*, "Lithium niobate piezo-optomechanical crystals," Optica **6**, 845 (2019).
32. W. Jiang, F. M. Mayor, R. N. Patel, *et al.*, "Nanobenders as efficient piezoelectric actuators for widely tunable nanophotonics at CMOS-level voltages," Commun. Phys. **3**, 156 (2020).
33. W. Jiang, C. J. Sarabalis, Y. D. Dahmani, *et al.*, "Efficient bidirectional piezo-optomechanical transduction between microwave and optical frequency," Nat. Commun. **11**, 1166 (2020).
34. L. Yang, S. Wang, M. Shen, *et al.*, "Controlling single rare earth ion emission in an electro-optical nanocavity," Nat. Commun. **14**, 1718 (2023).
35. R. Ge, X. Yan, Z. Liang, *et al.*, "Large quality factor enhancement based on cascaded uniform lithium niobate bichromatic photonic crystal cavities," Opt. Lett. **48**, 113 (2023).
36. R. Geiss, S. Diziain, R. Iliew, *et al.*, "Light propagation in a free-standing lithium niobate photonic crystal waveguide," Appl. Phys. Lett. **97**, 131109 (2010).
37. R. Geiss, S. Diziain, M. Steinert, *et al.*, "Photonic crystals in lithium niobate by combining focussed ion beam writing and ion-beam enhanced etching," Phys. Status Solidi A **10**, 211 (2014).
38. S. Diziain, R. Geiss, M. Zilk, *et al.*, "Second harmonic generation in free-standing lithium niobate photonic crystal L3 cavity," Appl. Phys. Lett. **103**, 051117 (2013).
39. S. Diziain, R. Geiss, M. Zilk, *et al.*, "Mode analysis of photonic crystal L3 cavities in self-suspended lithium niobate membranes," Appl. Phys. Lett. **103**, 251101 (2013).
40. R. Geiss, J. Brandt, H. Hartung, *et al.*, "Photonic microstructures in lithium niobate by potassium hydroxide-assisted ion beam-enhanced etching," J. Vac. Sci. Technol. B **33**, 010601 (2015).
41. V. Calero, M.-A. Suarez, R. Salut, *et al.*, "Toward highly reliable, precise, and reproducible fabrication of photonic crystal slabs on lithium niobate," J. Lightwave Technol. **37**, 698 (2019).
42. L. Qu, L. Bai, C. Jin, *et al.*, "Giant second harmonic generation from membrane metasurfaces," Nano Lett. **22**, 9652 (2023).
43. Z. Huang, K. Luo, Z. Feng, *et al.*, "Resonant enhancement of second harmonic generation in etchless thin film lithium niobate heteronanostructure," Sci. China Phys. Mech. Astron. **65**, 104211 (2022).
44. J. Zhang, B. Pan, W. Liu, *et al.*, "Ultra-compact electro-optic modulator based on etchless lithium niobate photonic crystal nanobeam cavity," Opt. Express **30**, 20839 (2022).
45. M. Ishikawa and M. Iwanaga, "In-plane second harmonic generations in photonic crystal slabs of $LiNbO_3$," Appl. Phys. Express **1**, 082101 (2008).
46. T. Wang, X. Xu, L. Yang, *et al.*, "Fabrication of lithium niobate fork grating by laser-writing-induced selective chemical etching," Nanophotonics **11**, 829 (2022).
47. T. Wang, X. Cheng, X. Li, *et al.*, "Femtosecond-laser-assisted high-aspect-ratio nanolithography in lithium niobate," Nanoscale **15**, 15298 (2023).
48. Q. Rolland, S. Dupont, J. Gazalet, *et al.*, "Simultaneous bandgaps in $LiNbO_3$ phoxonic crystal slab," Opt. Express **22**, 16288 (2014).
49. S. L. Li, "Transmission characteristics simulation of an erbium-doped lithium niobate film photonic crystal slab," Optik **124**, 6919 (2013).
50. P. Sivarajah, A. A. Maznev, B. K. Ofori-Okai, *et al.*, "What is the Brillouin zone of an anisotropic photonic crystal?" Phys. Rev. B **93**, 054204 (2016).
51. M. Minkov, I. A. D. Williamson, L. C. Andreani, *et al.*, "Inverse design of photonic crystals through automatic differentiation," ACS Photonics **7**, 1729 (2020).
52. Y. Li, C. Wang, and M. Loncar, "Design of nano-groove photonic crystal cavities in lithium niobate," Opt. Lett. **40**, 2902 (2015).
53. H. Jiang, H. Liang, R. Luo, *et al.*, "Nonlinear frequency conversion in one dimensional lithium niobate photonic crystal nanocavities," Appl. Phys. Lett. **113**, 021104 (2018).
54. H. Jiang, X. Yan, H. Liang, *et al.*, "High harmonic optomechanical oscillations in the lithium niobate photonic crystal nanocavity," Appl. Phys. Lett. **117**, 081102 (2020).
55. Y. Zhang, Y. Zhao, and R. Lv, "A review for optical sensors based on photonic crystal cavities," Sens. Actuators A **233**, 374 (2015).
56. Y. Akahane, T. Asano, B.-S. Song, *et al.*, "High-*Q* photonic nanocavity in a two-dimensional photonic crystal," Nature **425**, 944 (2003).
57. Y. Tanaka, T. Asano, and S. Noda, "Design of photonic crystal nanocavity with *Q*-factor of 10^9," J. Lightwave Technol. **26**, 1532 (2008).
58. R. Iliew, C. Etrich, T. Pertsch, *et al.*, "Slow-light enhanced collinear second-harmonic generation in two-dimensional photonic crystals," Phys. Rev. B **77**, 115124 (2008).
59. R. Iliew, C. Etrich, T. Pertsch, *et al.*, "Huge enhancement of backward second-harmonic generation with slow light in photonic crystals," Phys. Rev. B **81**, 023820 (2010).
60. J. Lu, J. B. Surya, X. Liu, *et al.*, "Periodically poled thin-film lithium niobate microring resonators with a second-harmonic generation efficiency of 250,000%/W," Optica **6**, 1455 (2019).
61. X. Yan, L. Ge, B. Zhu, *et al.*, "High optical damage threshold on-chip lithium tantalate microdisk resonator," Opt. Lett. **45**, 4100 (2020).
62. R. Ge, X. Liu, X. Yan, *et al.*, "Doubly resonant photonic crystal cavity using merged bound states in the continuum," Phys. Rev. B **107**, 165406 (2023).
63. X. Zhang, L. He, X. Gan, *et al.*, "Quasi-bound states in the continuum enhanced second-harmonic generation in thin-film lithium niobate," Laser Photonics Rev. **16**, 220031 (2022).
64. Z. Zheng, L. Xu, L. Huang, *et al.*, "Boosting second-harmonic generation in the metasurface using high- guided resonances and bound states in the continuum," Phys. Rev. B **106**, 125411 (2022).
65. S. Saravi, S. Diziain, M. Zilk, *et al.*, "Phase-matched second-harmonic generation in slow-light photonic crystal waveguides," Phys. Rev. A **92**, 063821 (2015).
66. S. Saravi, R. Quintero-Bermudez, F. Setzpfandt, *et al.*, "Effect of loss on slow-light-enhanced second-harmonic generation in periodic nanostructures," Opt. Lett. **41**, 3110 (2016).
67. S. Saravi, T. Pertsch, and F. Setzpfandt, "Generation of counterpropagating path-entangled photon pairs in a single periodic waveguide," Phys. Rev. Lett. **118**, 183603 (2017).
68. S. Saravi, T. Pertsch, and F. Setzpfandt, "Photonic crystal waveguides as sources of counterpropagating factorizable biphoton states," Opt. Lett. **44**, 69 (2019).

69. L. Zhao, M. Steinhart, M. Yosef, *et al.*, "Large-scale template-assisted growth of $LiNbO_3$ one-dimensional nanostructures for nano-sensors," Sens. Actuators B **109**, 86 (2005).
70. R. Luo, H. Jiang, H. Liang, *et al.*, "Self-referenced temperature sensing with a lithium niobate microdisk resonator," Opt. Lett. **42**, 1281 (2017).
71. Y. Xue, Z. Ruan, and L. Liu, "Electrode-free photonic electric field sensor on thin film lithium niobate with high sensitivity," Opt. Lett. **47**, 2097 (2022).
72. M.-P. Bernal, J. Amet, J. Safioui, *et al.*, "Pyroelectric control of the superprism effect in a lithium niobate photonic crystal in slow light configuration," Appl. Phys. Lett. **98**, 071101 (2011).
73. W. Qiu, H. Lu, F. I. Baida, *et al.*, "Ultra-compact on-chip slot Bragg grating structure for small electric field detection," Photonics Res. **5**, 212 (2017).
74. F. Zangeneh-Nejad and R. Fleury, "Topological fano resonances," Phys. Rev. Lett. **122**, 014301 (2019).
75. W. Qiu, A. Ndao, V. C. Vila, *et al.*, "Fano resonance-based highly sensitive, compact temperature sensor on thin film lithium niobate," Opt. Lett. **41**, 1106 (2016).
76. W. Qiu, A. Ndao, H. Lu, *et al.*, "Guided resonances on lithium niobate for extremely small electric field detection investigated by accurate sensitivity analysis," Opt. Express **24**, 20196 (2016).
77. V. Calero, M.-A. Suarez, R. Salut, *et al.*, "An ultra wideband-high spatial resolution-compact electric field sensor based on Lab-on-Fiber technology," Sci. Rep. **9**, 8058 (2019).
78. B. Robert, V. Calero, M.-A. Suarez, *et al.*, "Cost-efficient and high precision method for the assembly of LN-based photonic crystal slabs on the fiber tip for the implementation of E-field sensors," Opt. Mater. Express **11**, 2318 (2021).
79. X. Ma, C. Zhuang, R. Zeng, *et al.*, "Large-dynamic-range athermal lithium niobite on insulator/TiO_2 nanobeam electric field sensor," J. Phys. D Appl. Phys. **54**, 105101 (2020).
80. A. Hoblos, M. Suarez, N. Courjal, *et al.*, "Excitation of symmetry protected modes in a lithium niobate membrane photonic crystal for sensing applications," OSA Contin. **3**, 3008 (2020).
81. A. Panda, P. D. Pukhrambam, and G. Keiser, "Realization of sucrose sensor using 1D photonic crystal structure vis-à-vis band gap analysis," Microsyst. Technol. **27**, 833 (2021).
82. M. Xu, M. He, H. Zhang, *et al.*, "High-performance coherent optical modulators based on thin-film lithium niobate platform," Nat. Commun. **11**, 3911 (2020).
83. M. Xu, Y. Zhu, F. Pittalà, *et al.*, "Dual-polarization thin-film lithium niobate in-phase quadrature modulators for terabit-per-second transmission," Optica **9**, 61 (2022).
84. H. Lu, W. Qiu, C. Guyot, *et al.*, "Optical and RF characterization of a lithium niobate photonic crystal modulator," IEEE Photon. Technol. Lett. **26**, 1332 (2014).
85. Y. Qi, Z. Zhang, W. Jia, *et al.*, "Design of ultracompact high-speed-integrated lithium-niobate periodic dielectric waveguide modulator," Adv. Photonics Res. **3**, 2200050 (2022).
86. C. Deng, L. Zhu, M. Lu, *et al.*, "Design and simulation of high modulation efficiency, low group velocity dispersion lithium niobate slow-wave electro-optic modulator based on a fishbone-like grating," Opt. Laser. Technol. **158**, 108769 (2023).
87. Y. Zhang, H. Tian, D. Yang, *et al.*, "Ultra-compact low-voltage and slow-light MZI electro-optic modulator based on monolithically integrated photonic crystal," Opt. Commun. **315**, 138 (2013).
88. G. W. Burr, S. Diziain, and M.-P. Bernal, "The impact of finite-depth cylindrical and conical holes in lithium niobate photonic crystals," Opt. Express **16**, 6302 (2008).
89. O. Yavuzcetin, B. Ozturk, D. Xiao, *et al.*, "Conicity and depth effects on the optical transmission of lithium niobate photonic crystals patterned by focused ion beam," Opt. Mater. Express **1**, 1262 (2011).
90. Q. Z. Zhao, Z. B. Zhang, J. Q. Xu, *et al.*, "Hole geometry effect on stop-band characteristics of photonic crystal in Ti-diffused $LiNbO_3$ waveguide," Mater. Chem. Phys. **186**, 498 (2017).
91. Q. Z. Zhao and D. L. Zhang, "Transmission spectral characteristics of photonic crystals milled in annealed proton-exchange $LiNbO_3$ waveguide," Chin. Phys. Lett. **34**, 034207 (2017).
92. H.-F. Wang, S. K. Gupta, X.-Y. Zhu, *et al.*, "Bound states in the continuum in a bilayer photonic crystal with TE-TM cross coupling," Phys. Rev. B **98**, 214101 (2018).
93. Z. Li, R. N. Wang, G. Lihachev, *et al.*, "Tightly confining lithium niobate photonic integrated circuits and lasers," arXiv:2208.05556 (2022).
94. C.-H. Hou, M.-P. Bernal, C.-C. Chen, *et al.*, "Purcell effect observation in erbium doped lithium niobate photonic crystal structures," Opt. Commun. **281**, 4151 (2008).
95. Y. Liu, X. Yan, J. Wu, *et al.*, "On-chip erbium-doped lithium niobate microcavity laser," Sci. China Phys. Mech. Astron. **64**, 234262 (2021).
96. Q. Luo, Z. Hao, C. Yang, *et al.*, "Microdisk lasers on an erbium-doped lithium-niobite chip," Sci. China Phys. Mech. Astron. **64**, 234263 (2021).
97. T. Li, K. Wu, M. Cai, *et al.*, "A single-frequency single-resonator laser on erbium-doped lithium niobate on insulator," APL Photonics **6**, 101301 (2021).
98. Z.-W. Yan, Q. Wang, M. Xiao, *et al.*, "Probing rotated Weyl physics on nonlinear lithium niobate-on-insulator chips," Phys. Rev. Lett. **127**, 013901 (2021).
99. S. Duan, Y. Chen, G. Li, *et al.*, "Broadband polarization beam splitter based on a negative refractive lithium niobate photonic crystal slab," Chin. Opt. Lett. **14**, 042301 (2016).
100. C. Lu, B. Zhu, C. Zhu, *et al.*, "All-optical logic gates and a half-adder based on lithium niobate photonic crystal micro-cavities," Chin. Opt. Lett. **17**, 072301 (2019).
101. J. Jin, X. Yin, L. Ni, *et al.*, "Topologically enabled ultrahigh-Q guided resonances robust to out-of-plane scattering," Nature **574**, 501 (2019).